Defect-Induced Vibration Modes of Ar^+-Irradiated MoS_2

Soungmin Bae,[1] Natsuki Sugiyama,[1] Takatoshi Matsuo,[1] Hannes Raebiger,[1,*] Ken-ichi Shudo,[1,2,†] and Koichi Ohno[3,4]

[1]*Department of Physics, Yokohama National University, Hodogaya-ku, Yokohama 240-8501, Japan*
[2]*The Center for Sustainable Resource Science and Elements Chemistry Laboratory, The Institute of Physical and Chemical Research (RIKEN), Saitama 351-0198, Japan*
[3]*Institute for Quantum Chemical Exploration (IQCE), Minato-ku, Tokyo 108-0022, Japan*
[4]*Department of Chemistry, Graduate School of Science, Tohoku University, Aoba-ku, Sendai 980-8578, Japan*

(Received 12 April 2016; revised manuscript received 24 August 2016; published 6 February 2017)

The Ar^+-irradiated molybdenum-disulfide (MoS_2) surface is studied by means of Raman spectroscopy and first-principles calculation. This experimental study reveals that Ar^+ irradiation gives rise to satellite peaks at the lower-frequency side of the Raman-active E^1_{2g} and A_{1g} modes of MoS_2 and a new peak at approximately 450 cm^{-1}. We calculate the phonon modes and Raman spectra of defective MoS_2 systems from first principles, and show that Mo and S vacancies give rise to such satellite peaks. These satellite peaks are a modulation of the E^1_{2g} and A_{1g} modes, described in terms of localization and scattering of vibration modes. The new peak at 450 cm^{-1}, however, is a unique signature of the S vacancy. At low irradiation doses, the S vacancy is the dominant defect, whereas for large irradiation doses, the satellite peaks overshadow the MoS_2 peaks, which we show to be typical for the Mo vacancy and MoS_6 vacancy cluster. We thus show that Raman spectroscopy can be used not only to observe defects in two-dimensional materials, but also to identify the type of the defects.

DOI: 10.1103/PhysRevApplied.7.024001

I. INTRODUCTION

Since the discovery of graphene, two-dimensional materials have attracted increasing attention due to their unique properties [1,2]. Although graphene has many outstanding properties for devices, its zero band gap is a drawback for practical applications. Transition-metal dichalcogenides, mostly MoS_2, WS_2, and WTe_2, have been suggested as promising materials for two-dimensional devices due to their relatively large band gap, weak interlayer interaction, and high mobility [3–5]. Based on few-layered MoS_2, several prototype devices have been demonstrated such as the field-effect transistor, nanoribbons, and the thin-film transistor [4,6,7]. However, defect formation is often inevitable in the fabrication and observation processes of such device structures, and device performance depends crucially on the abundance and types of defects present in the material [8–11]. For instance, a field-effect transistor fabricated of defective MoS_2 shows a gross performance decrement in its on-to-off ratio and carrier mobility [8–10], because electronic decay is nonlinearly affected by phonon scattering due to the defects [9,11,12]. On the other hand, as in any semiconductor devices, defect engineering can be used to control the conductivity nature (n or p type) and the Fermi-level position [13,14], and defects may even introduce new functionalities, e.g., by inducing magnetism [15]. This has motivated several studies of artificially defective MoS_2 samples [13,15,16], but the nature and microscopy of the intentionally or unintentionally created defects remains poorly understood. Thus, a simple and noninvasive technique to observe and identify defects in two-dimensional materials and/or devices is highly desirable.

Raman scattering spectroscopy is a prominent tool to explore the mechanical and electronic properties of layered materials [5,17,18]. It probes lattice vibrations, and, thus, any alternations in the material that affect its vibrational modes can be probed by it. For instance, shear and breathing modes are sensitive to the number of monolayers [19], so Raman scattering is a noninvasive probe for the number of monolayers in few-layer transition-metal dichalcogenides and trichalgogenides [20,21]. For graphene, the intensity ratio of the D and G peaks in Raman spectra measures the concentration of lattice defects [17,22,23]. Likewise, variations in Raman spectra of MoS_2 upon ion irradiation [16,18,24] may be signatures of certain types of defects. Indeed, a redshift in the E' mode and a blueshift in the A'_1 mode indicate the presence of S vacancies in MoS_2 [25–27]. However, in addition to such rather small peak shifts, defects may induce completely new vibration modes with unique signatures in Raman spectra, which remain to be explored.

In this article, we investigate Ar^+-irradiated MoS_2 surfaces by means of Raman spectroscopy and first-principles calculation. In our Raman observation, we find

*hannes@ynu.ac.jp
†ken1@ynu.ac.jp

that after Ar^+ irradiation, defect-induced satellites appear nearby the Raman-active A_{1g} and E^1_{2g} modes of MoS_2. The Raman intensity of the defect-induced peaks increases when Ar^+ doses are increased. We report the results of first-principles calculations on the defective monolayer systems of MoS_2 to demonstrate Raman activities under the first-order Raman process for the defect-induced vibration modes. The insight, based on the comparison of the calculated alternation of the Raman spectra with the experimental data, would bring chemical and physical researchers a method for the analysis of defective structures of two-dimensional materials.

II. RAMAN OBSERVATION OF Ar^+-IRRADIATED MoS_2 SURFACES

We prepare two kinds of MoS_2 samples. The first samples are prepared by mechanical exfoliation from the surface of MoS_2 crystal using adhesive tape in the atmosphere; these samples are referred to as *bulk* since their thickness is several microns. These cleaved MoS_2 are attached on a silicon substrate (17.3×7.9 mm^2) with sliver paste, and the system can be heated by passing direct current through the silicon substrate in an ultrahigh vacuum (UHV) chamber. All the samples are first degassed at 538 K for 30 min in UHV to prepare a clean and contamination-free substrate. The second type of samples are made from MoS_2 powders (the average diameter is 3–5 μm) chemically exfoliated through intercalation in a hexane solution of BuLi, as described in Refs. [28,29]. Mono- to few-layer domains appear after drying the colloidal solution of the exfoliated MoS_2 onto SiO_2 substrate. Then these samples are irradiated by Ar^+ ions at the energy of 500 eV in the UHV. Ar^+ irradiation is carried out with fluences of 5.65×10^{14} and 2.26×10^{15} ions/cm^2, estimated from the ion current and irradiation times. The incident angle of Ar^+ is within $\pm 2°$ from the normal to the surface of the bulk samples, i.e., the electric field is applied perpendicular to the MoS_2 layer. After the irradiation process, residual argon is removed from the samples by heating at 583 K for one hour. Before and after irradiation, samples are observed by Raman scattering spectroscopy in the backscattering geometry using a micro-Raman scope (inVia Reflex, Renishaw; equipped with an *N Plan EPI* ×50 objective lens whose numerical aperture is 0.75) with an excitation laser at the wavelength of 532 nm. It should be noted, however, that the chemically exfoliated MoS_2 flakes are skewed from the normal incidence in the Raman measurement, because the flakes are on the thin solid compound of residual lithium remaining on the substrate.

The Raman spectra change with the Ar^+ dose on the MoS_2 surface, as shown in Fig. 1. On a pristine bulk MoS_2 surface, two typical Raman-active peaks, i.e., the A_{1g} and E^1_{2g} peaks, are clearly seen at 387 and 412 cm^{-1}, respectively. After Ar^+ irradiation, additional broad

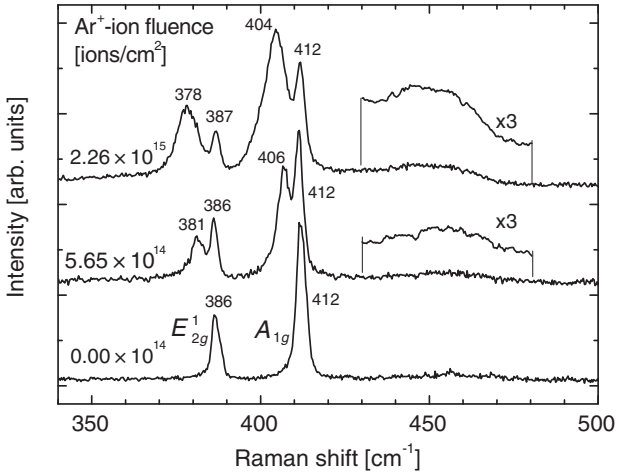

FIG. 1. Raman spectra of pristine bulk MoS_2 (bottom) and Ar^+-irradiated bulk MoS_2 at fluences of 5.65×10^{14} ions/cm^2 (middle) and 2.26×10^{15} ions/cm^2 (top).

satellite peaks appear in the lower-frequency side of both the E^1_{2g} and A_{1g} peaks. The Raman intensity of these satellite peaks increases when the Ar^+ dose increases. This indicates that the new peaks are induced by lattice defects introduced by the Ar^+ irradiation. The maxima of the defect-induced peaks in the lower-frequency side of E^1_{2g} and A_{1g} peaks are at 377–381 and 404–406 cm^{-1}, respectively.

Similar satellite peaks have been previously observed in defective MoS_2 samples [15,16,18], and were rationalized by resonance and finite-crystal size effects. In the resonance-effect model, defect-induced peaks are assigned to E^2_{1u} and B_{1u} modes, which are Davydov pairs of E^1_{2u} and A_{1g} modes observed by Sekine *et al.* [24] in resonance Raman spectroscopy. However, these resonance peaks can be observed only when the incident photon energy is tuned to the exciton energies of MoS_2, which is not the case in ordinary Raman scattering spectroscopies (such as ours) using the same light source at the off-resonant photon energy. On the other hand, the finite-crystal size effect (cf. Raman spectra of Si nanocrystals [18,30]) allows phonons with $q \neq 0$ to be visible in Raman spectra due to the loosening of the Raman selection rule by periodicity breaking. This would lead to a softening (redshift) of the E^1_{2g} and hardening (blueshift) of the A_{1g} peaks due to these $q \neq 0$ phonons manifested by a spreading of the peaks (E^1_{2g} towards lower frequencies and A_{1g} towards higher frequencies) [31]. Our observation clearly does not show such trends, but instead, new sharp satellite peaks emerge at the lower-frequency sides of the E^1_{2g} and A_{1g} peaks. Thus, neither of the previous models correctly describes the new defect-associated Raman peaks that appear upon ion irradiation.

Next, in our Raman spectra of the bilayer system shown in Fig. 2, peaks of the pristine sample are at 386 and

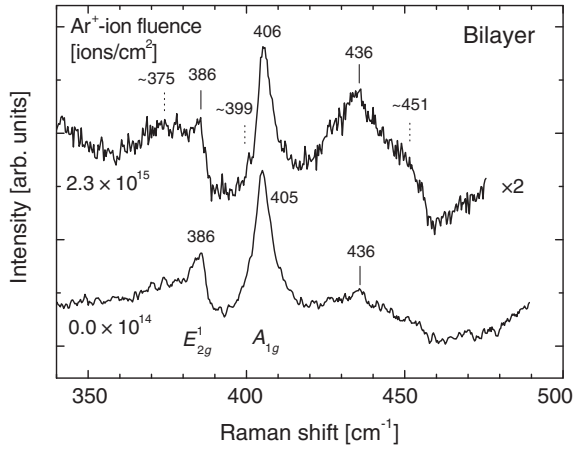

FIG. 2. Raman spectra of chemically exfoliated bilayer MoS_2 flakes before (bottom) and after Ar^+ irradiation at the fluence of 2.3×10^{15} ions/cm^2 (top). Notice that the bilayer intensity is multiplied by a factor of 2 (×2) due to the weakening of the Raman signal.

434 cm^{-1} for the A_{1g} and E^1_{2g} modes, respectively. Notice that the peaks are not as sharp as for the bulk cases as the signal is very weak, and that there is also a broad peak at 436 cm^{-1}. Upon irradiation, also the bilayer system shows the emergence of new defect-induced vibration modes. A broad new peak emerges at approximately 373 cm^{-1}, which is shifted by approximately 10 cm^{-1} from the E^1_{2g} peak. This is the same defect-induced peak as is observed for the bulk system. The broad feature at 435 cm^{-1} is relatively enhanced. In the monolayer domain of the chemically exfoliated samples, no clear signals corresponding to either the E' or the A'_1 modes are found after irradiation, indicating that the Ar^+ irradiation destroyed our monolayer MoS_2 flakes.

III. PHONON VIBRATION MODES OF DEFECTIVE MoS_2 SURFACES AND THEIR RAMAN SPECTRA

To identify the irradiation-induced defects in the MoS_2 surfaces, we perform a first-principles calculation of MoS_2 monolayer models containing vacancy-type defects. We construct a 5×5 monolayer slab model (Fig. 3), and consider three typical vacancy structures: the Mo vacancy, the S vacancy, and the MoS_6 vacancy cluster, as shown in Fig. 3, panels (c)–(e). Vacuum spacing between periodic images of the monolayer slab is set to 20 Å to avoid spurious interaction. Electronic structure and vibrational properties are calculated using the Vienna *ab initio* simulation package (VASP) code [32], based on density functional theory with the local-density approximation for exchange and correlation and the projector-augmented wave method. The plane-wave cutoff is set as 500 eV and the first Brillouin zone is sampled by a $3 \times 3 \times 1$ Monkhorst-Pack $\vec{k}$-points grid. The force criterion for structural relaxation is 10^{-4} eV/Å. After obtaining the relaxed structures, the harmonic force constants are calculated within frozen phonon approximation, and normal vibration modes are obtained through diagonalization of the dynamical matrix. Raman tensors $\tilde{\alpha}$ are obtained with the Raman off-resonant activity calculator using VASP as a back end [33], and the polarizability tensor is calculated using a polarizability routine of the VASP code [34]. The spectral Raman intensities are then calculated as $\tilde{\alpha}^2_{xx} + \tilde{\alpha}^2_{xy} + \tilde{\alpha}^2_{yx} + \tilde{\alpha}^2_{yy}$ corresponding to our optical backscattering geometry.

We first calculate phonon vibration modes and their Raman intensities for the pristine monolayer MoS_2 shown in Fig. 4. There are two Raman-active modes, the E' mode and the A'_1 mode, which are typically observed in Raman spectroscopy of MoS_2. The E' mode is an in-plane vibration mode and the A'_1 mode is an out-of-plane vibration mode, as shown in the insets. The calculated frequencies, 391.7 and 408.5 cm^{-1}, are in good agreement with previous theories and experiment [15,20,35]. Notice that the monolayer vibration modes E' and A'_1 correspond to bulk or few-layer modes E^1_{2g} and A_{1g}. The labeling is different due to different symmetry in the direction perpendicular to the surface. It turns out that the defect-induced vibration modes (discussed below) are confined within one monolayer even in bulk systems, so for the sake

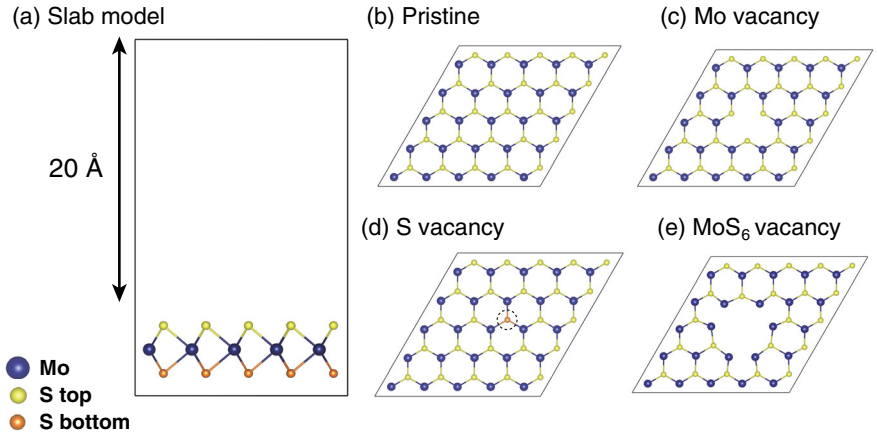

FIG. 3. (a) The slab model of the 5×5 monolayer MoS_2. The slab model is extended from the primitive cell in plane. The top views are of (b) pristine, (c) Mo vacancy, (d) S vacancy, and (e) MoS_6 vacancy structures. Each vacancy is placed at the center of the slab model.

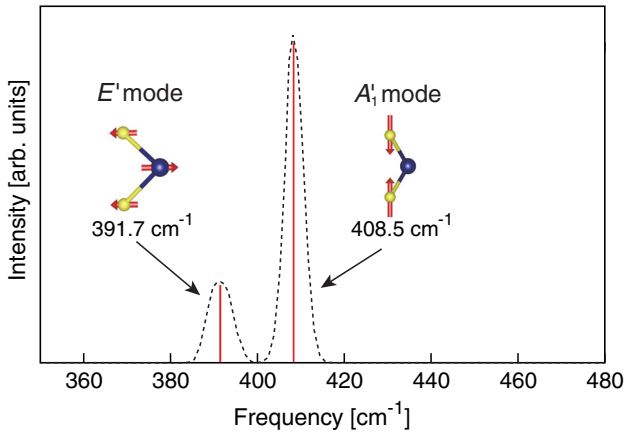

FIG. 4. Calculated Raman spectra of monolayer pristine MoS_2. The insets show normal displacements and their vibration frequency of the E^1_{2g} mode and the A_{1g} mode. The envelope of the calculated Raman spectra is evaluated by smearing the peaks with half width of 5 cm^{-1}.

of simplicity, we henceforth collectively refer to both bulk and monolayer modes as E and A modes. Our calculated Raman spectra quantitatively well describe the intensity ratio between the E and A modes. Because our experiment and calculation of Raman spectra are in the backscattering geometry, the A mode has a larger intensity than the E mode. This intensity ratio can be changed with respect to the direction of polarizations due to anisotropy of the Raman tensor [18].

Next, we consider the Raman spectra of the defective systems. Figure 5 shows the calculated lattice vibration and Raman intensity for the Mo-vacancy, S-vacancy, and MoS_6-vacancy cluster [panels (c)–(e) in Fig. 3]. When vacancies are introduced, calculated Raman spectra show remarkable changes. For all vacancies, Raman spectra show defect-induced peaks in the lower-frequency sides of the E^1_{2g} and A_{1g} modes. We carry out test calculations of the same defects in a $3 \times 3 \times 2$ bulk supercell, given in the Supplemental Material [36]. Even for this laterally small 3×3 system we observe similar defect-induced vibration modes. It is important to note that in the bulk calculation, defect-induced vibrations are confined within the defective layer, i.e., these modes can equally well be described in a monolayer system, which allows us to use the laterally larger 5×5 slab. Thus, we may well compare monolayer calculations with bulk experiment, or vice versa. This is further confirmed by our bilayer experiment, where the defect-induced peak downshifted from the E mode appears essentially at the same frequency as in the bulk experiment, i.e., this defect-induced peak is hardly affected by reducing sample thickness.

The calculated Raman spectra are different for the various vacancies. We begin by discussing the vibration modes related to the S vacancy [Fig. 5(b)]. The perturbation derived from the S vacancy is relatively small, manifested by the fact that the E' mode [Fig. 5(b), peak 2] and A'_1 mode [Fig. 5(b), peak 4] of pristine MoS_2 remain in the Raman spectrum of the defective system, i.e., the defect-induced satellite peaks coexist with the pristine MoS_2 Raman peaks. The Raman intensities of pristine MoS_2 E' and A'_1 modes are still larger than those of their defect-induced satellite peaks. However, in the case of the Mo vacancy and the MoS_6 vacancy cluster, the Raman intensities of E^1_{2g} and A_{1g} modes are significantly decreased and become overshadowed by defect-induced Raman peaks, which appear with large Raman intensities. This large perturbation on lattice vibration in contrast to the S vacancy is natural since Mo is much heavier than S. It follows that the Mo and MoS_6 vacancies hardly affect the intensity ratio (I_A/I_E). For the S vacancy, however, the intensity of the A_{1g} mode (peak 4) is diminished compared with that of the E^1_{2g} mode (peak 2). This explains our experiment, where I_A/I_E changed from 2.44 to 2.3 when the Ar^+ dose increases from 0 to 2.26×10^{15} ions/cm^2 for bulk samples [37]. Thus, the missing S atoms result in the relative decrease of A_{1g} components without destroying the pristine A'_1 and E' modes. A similar change in the intensity ratio between the E^1_{2g} and A_{1g} modes (I_A/I_E) has been observed in various Raman experiments [15,16].

The atomic displacements of calculated lattice vibrations are illustrated in the right-hand panels of Fig. 5 corresponding to the Raman spectra on the left-hand side. In the case of defect-induced peaks downshifted from the E' mode by approximately 9 cm^{-1}, atoms mostly move within the surface plane [peak 1 in panel (a), peaks 1 and 2 in (b), and peak 1 in (c)], which indicates that defect-induced Raman peaks perturbed from the E' mode remain in-plane vibrations. These modes are silent modes in pristine crystal, and are Raman activated due to the symmetry reduction by the lattice perturbation effect on the plain phonon. On the other hand, the defect-induced peaks around A'_1 modes are lattice vibrations where atoms move mostly perpendicular to the surface plane [peaks 2–4 in panel (a), peaks 3–5 in (b), and peaks 2–4 in (c)], namely, the out-of-plane direction.

The localization of the defect-induced in-plane and out-of-plane vibration modes is strikingly different, as illustrated in Fig. 6. For the defect-induced in-plane modes near the E' mode, the atoms around the vacancy have a small vibration amplitude, while the more distant atoms have a larger amplitude. The out-of-plane vibrations near the A'_1 mode, on the other hand, are strongly localized around the vacancy; atoms next to vacancy have large amplitude while the more distant atoms hardly move. This indicates that the in-plane lattice vibration, originated from the E^1_{2g} mode, propagates the pristine area, and is scattered at the vacancy acting as the center of perturbation. For the A_{1g}-originated vibrations, in turn, the vacancy confines the out-of-plane lattice vibration, playing as the localization center.

We turn our attention to the broad Raman peak that for bulk samples appears in the frequency region from

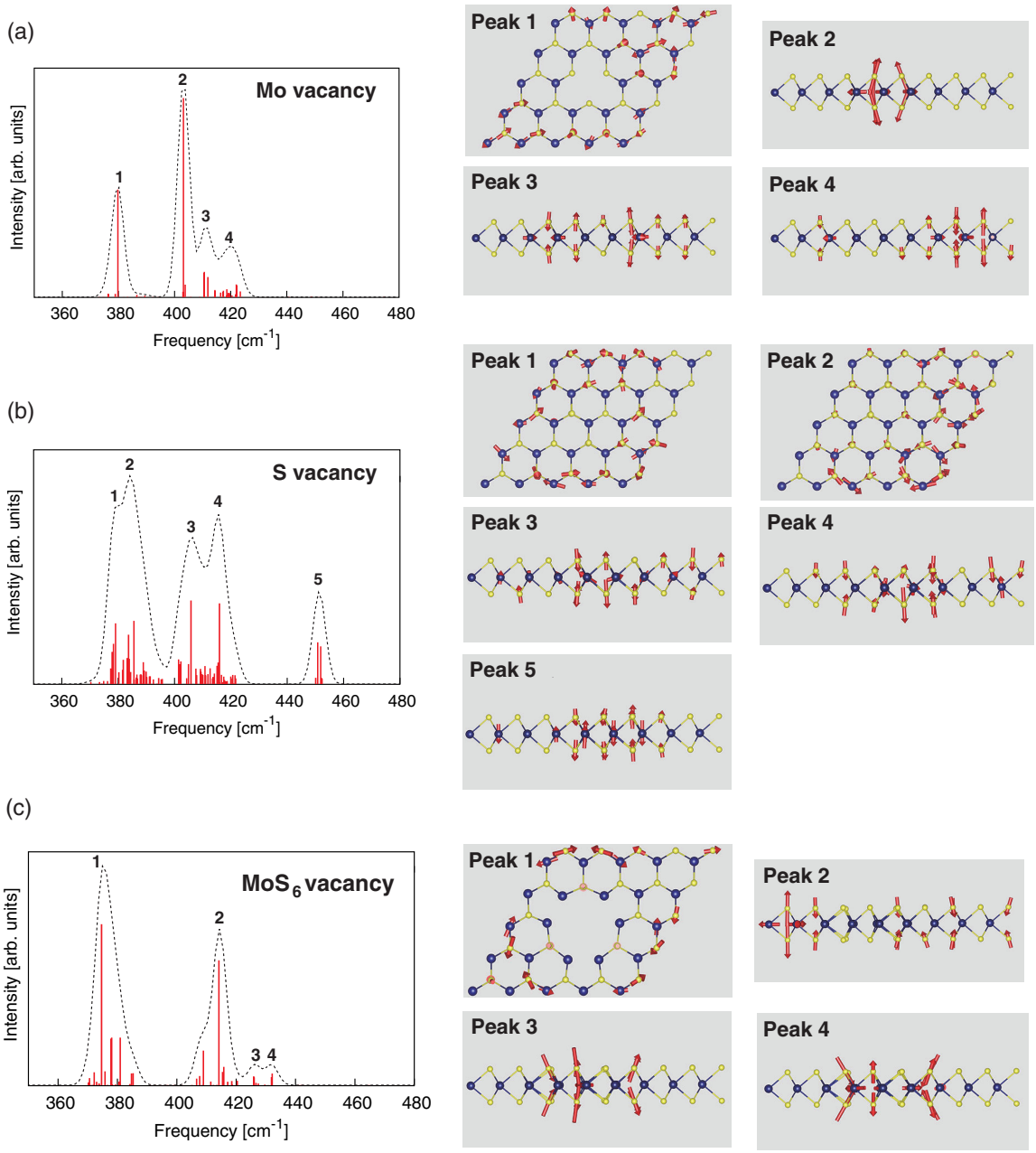

FIG. 5. Calculated Raman spectra and lattice vibrations of defective MoS_2 with (a) Mo vacancy, (b) S vacancy, and (c) MoS_6 vacancy cluster. Envelopes of each Raman spectra are evaluated by smearing the peaks with half width 5 cm^{-1}. Calculated Raman peaks are labeled by numbers and each associated lattice vibration is illustrated in the right column. Note that the displacements in plane along the surface are top viewed, while those out of plane are side viewed.

440–460 cm^{-1} only after the Ar^+ irradiation (Fig. 1). In the calculation, such a feature only appears in the Raman spectrum for the S vacancy [peak 5 in Fig. 5(b)], and thus can be dubbed as a unique signature of the S vacancy. Other defect-induced Raman peaks appear in the lower-frequency side of the E and A modes, and can be described as satellite peaks attributed to any of the considered vacancy defects based on the frequency information. At a low Ar^+-irradiation dose (middle curve in Fig. 1), the experimental Raman spectrum (including peak intensity) is well described by the calculation of the S vacancy. The appearance of the peak around 440–460 cm^{-1} combined with the change in the intensity ratio (I_A/I_E), confirms that the dominant defect at the low irradiation dose is the S vacancy, consistent with previous reports [38,39]. This suggests that initially S atoms are preferably removed from the system, because it is lighter than Mo, and the S vacancy has a low formation energy [40]. At a larger Ar^+-irradiation

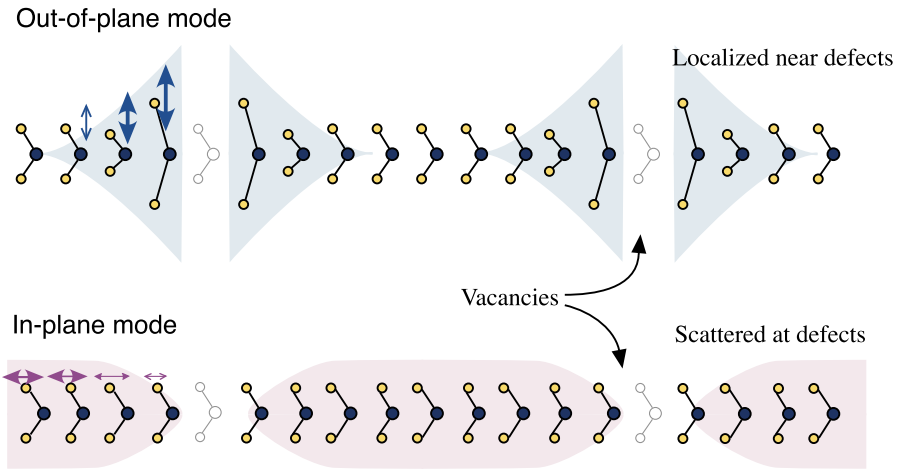

FIG. 6. Spatial distribution of the atomic displacements schematically shown in in-plane and out-of-plane modes. The background colored envelopes show the amplitude of the displacement. The in-plane mode has a weak amplitude near the vacancy while the out-of-plane mode only has amplitude adjacent to the vacancy (cf. the right-hand columns in Fig. 5 for each mode).

dose (top curve in Fig. 1), the satellite peaks in the low-frequency side of the E^1_{2g} and A_{1g} modes overshadow the main peaks, which indicates also the presence of the Mo vacancy. Moreover, the shift to the lower frequency of the satellite of E^1_{2g} indicates larger cluster removal, such as the MoS_6 vacancy. The intensity ratio I_A/I_E, frequency of satellite of E^1_{2g}, and the new feature in the 440–460 cm^{-1} region are fingerprints of defect formation, and provide information on the specific type of defects formed.

Finally, we note the bilayer experiment clouded by the additional peak at 435 cm^{-1}. This peak is present even before irradiation. The MoS_6 vacancy cluster exhibits additional Raman peaks in this region [Fig. 5, peaks 3 and 4 in panel (c)], which suggests that vacancy clusters such as the MoS_6 vacancy are formed already during the chemical exfoliation. Relative enhancement of this feature by the Ar^+ irradiation is due to further MoS_6 vacancy cluster formation. This coincidence again indicates the usefulness of calculating Raman spectra from first principles to assign spectral profiles to defected samples.

IV. SUMMARY

We show that lattice defects in MoS_2 give rise to new Raman-active vibration modes. In the experimental Raman observation of defective MoS_2 systems, defect-induced satellite peaks appear in the low-frequency side of E^1_{2g} and A_{1g} modes of MoS_2, which is well reproduced by first-principles calculation of MoS_2 systems containing Mo vacancies, S vacancies, or MoS_6 vacancy clusters. The change of the intensity ratio between E^1_{2g} and A_{1g} peaks (I_A/I_E) is attributed to a small perturbation derived from the S vacancy. The defective MoS_2 systems exhibit a new vibration mode at around 440–460 cm^{-1}, which by our calculation is identified as a unique signature of the S vacancy. The intensity of the satellite peaks increases along with an increase in the irradiation dose, and their possible dominance over the E^1_{2g} and A_{1g} modes of pristine MoS_2 indicates the formation of Mo vacancies or MoS_6 vacancy clusters. The lower shift of the satellites of the E^1_{2g} mode implies the formation of the large cluster vacancy. We thus show that Raman spectroscopy, together with first-principles calculation, is a powerful tool to identify various types of defects in two-dimensional systems.

ACKNOWLEDGMENTS

S. B. thanks the Rotary Yoneyama Memorial Foundation for support. Calculations are done partly at the facility of the Supercomputer Center of the Institute for Solid State Physics, University of Tokyo. This work is supported by JSPS Grant-in-Aid for Challenging Exploratory Research, Grant No. 24655007 and Grant-in-Aid for Scientific Research (C), Grant No. 16K04992.

[1] K. S. Novoselov, D. Jiang, F. Schedin, T. J. Booth, V. V. Khotkevich, S. V. Morozov, and A. K. Geim, Two-dimensional atomic crystals, Proc. Natl. Acad. Sci. U.S.A. **102**, 10451 (2005).
[2] M. J. Allen, V. C. Tung, and R. B. Kaner, Honeycomb carbon: A review of graphene, Chem. Rev. **110**, 132 (2010).
[3] K. F. Mak, C. Lee, J. Hone, J. Shan, and T. F. Heinz, Atomically Thin MoS_2: A New Direct-Gap Semiconductor, Phys. Rev. Lett. **105**, 136805 (2010).
[4] B. Radisavljevic, A. Radenovic, J. Brivio, V. Giacometti, and A. Kis, Single-layer MoS_2 transistors, Nat. Nanotechnol. **6**, 147 (2011).
[5] R. Ganatra and Q. Zhang, Few-layer MoS_2: A promising layered semiconductor, ACS Nano **8**, 4074 (2014).
[6] S. Kim, A. Konar, W.-s. Hwang, J. H. Lee, J. Lee, J. Yang, C. Jung, H. Kim, J.-b. Yoo, J.-Y. Choi, Y. W. Jin, S. Y. Lee, D. Jena, W. Choi, and K. Kim, High-mobility and low-power thin-film transistors based on multilayer MoS_2 crystals, Nat. Commun. **3**, 1011 (2012).
[7] A. Castellanos-Gomez, M. Barkelid, A. M. Goossens, V. E. Calado, H. S. J. Van Der Zant, and G. A. Steele, Laser-thinning of MoS_2: On demand generation of a single-layer semiconductor, Nano Lett. **12**, 3187 (2012).

[8] H. Qiu, T. Xu, Z. Wang, W. Ren, H. Nan, Z. Ni, Q. Chen, S. Yuan, F. Miao, F. Song, G. Long, Y. Shi, L. Sun, J. Wang, and X. Wang, Hopping transport through defect-induced localized states in molybdenum disulphide, Nat. Commun. **4**, 2642 (2013).

[9] W. Zhu, T. Low, Y.-H. Lee, H. Wang, D. B. Farmer, J. Kong, F. Xia, and P. Avouris, Electronic transport and device prospects of monolayer molybdenum disulphide grown by chemical vapour deposition, Nat. Commun. **5**, 3087 (2014).

[10] M. R. Islam, N. Kang, U. Bhanu, H. P. Paudel, M. Erementchouk, L. Tetard, M. N. Leuenberger, and S. I. Khondaker, Tuning the electrical property via defect engineering of single layer MoS_2 by oxygen plasma, Nanoscale **6**, 10033 (2014).

[11] C. Durand, X. Zhang, J. Fowlkes, S. Najmaei, J. Lou, and A.-P. Li, Defect-mediated transport and electronic irradiation effect in individual domains of CVD-grown monolayer MoS_2, J. Vac. Sci. Technol. B **33**, 02B110 (2015).

[12] J. H. Strait, P. Nene, and F. Rana, High intrinsic mobility and ultrafast carrier dynamics in multilayer metal-dichalcogenide MoS_2, Phys. Rev. B **90**, 245402 (2014).

[13] A. Inoue, T. Komori, and K. Shudo, Atomic-scale structures and electronic states of defects on Ar^+-ion irradiated MoS_2, J. Electron Spectrosc. Relat. Phenom. **189**, 11 (2013).

[14] R. Murray, K. Haynes, X. Zhao, S. Perry, C. Hatem, and K. Jones, The effect of low energy ion implantation on MoS_2, ECS J. Solid State Sci. Technol. **5**, Q3050 (2016).

[15] S. Mathew, K. Gopinadhan, T. K. Chan, X. J. Yu, D. Zhan, L. Cao, A. Rusydi, M. B. H. Breese, S. Dhar, Z. X. Shen, T. Venkatesan, and J. T. L. Thong, Magnetism in MoS_2 induced by proton irradiation, Appl. Phys. Lett. **101**, 102103 (2012).

[16] L. Guardia, J. I. Paredes, R. Rozada, S. Villar-Rodil, A. Martínez-Alonso, and J. M. D. Tascón, Production of aqueous dispersions of inorganic graphene analogues by exfoliation and stabilization with non-ionic surfactants, RSC Adv. **4**, 14115 (2014).

[17] A. C. Ferrari, Raman spectroscopy of graphene and graphite: Disorder, electron-phonon coupling, doping and non-adiabatic effects, Solid State Commun. **143**, 47 (2007).

[18] X. Zhang, X.-F. Qiao, W. Shi, J.-B. Wu, D.-S. Jiang, and P.-H. Tan, Phonon and Raman scattering of two-dimensional transition metal dichalcogenides from monolayer, multilayer to bulk material, Chem. Soc. Rev. **44**, 2757 (2015).

[19] X. Zhang, W. P. Han, J. B. Wu, S. Milana, Y. Lu, Q. Q. Li, A. C. Ferrari, and P. H. Tan, Raman spectroscopy of shear and layer breathing modes in multilayer MoS_2, Phys. Rev. B **87**, 115413 (2013).

[20] A. Molina-Sánchez and L. Wirtz, Phonons in single-layer and few-layer MoS_2 and WS_2, Phys. Rev. B **84**, 155413 (2011).

[21] K. Osada, S. Bae, M. Tanaka, H. Raebiger, K. Shudo, and T. Suzuki, Phonon properties of few-layer crystals of quasi-one-dimensional ZrS_3 and $ZrSe_3$, J. Phys. Chem. C **120**, 4653 (2016).

[22] E. B. Barros, K. Sato, G. G. Samsonidze, A. G. Souza Filho, M. S. Dresselhaus, and R. Saito, D band Raman intensity calculation in armchair edged graphene nanoribbons, Phys. Rev. B **83**, 245435 (2011).

[23] M. Choi, J. Son, H. Choi, H.-j. Shin, S. Lee, S. Kim, S. Lee, S. Kim, K.-R. Lee, J. Kim, and H. Hong, In situ Raman spectroscopy of current-carrying graphene microbridge, J. Raman Spectrosc. **45**, 168 (2014).

[24] T. Sekine, K. Uchinokura, T. Nakashizu, E. Matsuura, and R. Yoshizaki, Dispersive Raman mode of layered compound $2H$-MoS_2 under the resonant condition, J. Phys. Soc. Jpn. **53**, 811 (1984).

[25] S. Mignuzzi, A. J. Pollard, N. Bonini, B. Brennan, I. S. Gilmore, M. A. Pimenta, D. Richards, and D. Roy, Effect of disorder on Raman scattering of single-layer MoS_2, Phys. Rev. B **91**, 195411 (2015).

[26] W. M. Parkin, A. Balan, L. Liang, P. M. Das, M. Lamparski, C. H. Naylor, J. A. Rodríguez-Manzo, A. T. C. Johnson, V. Meunier, and M. Drndić, Raman shifts in electron-irradiated monolayer MoS_2, ACS Nano **10**, 4134 (2016).

[27] Z. Lin, B. R. Carvalho, E. Kahn, R. Lv, R. Rao, H. Terrones, M. A. Pimenta, and M. Terrones, Defect engineering of two-dimensional transition metal dichalcogenides, 2D Mater. **3**, 022002 (2016).

[28] G. Eda, H. Yamaguchi, D. Voiry, T. Fujita, M. Chen, and M. Chhowalla, Photoluminescence from chemically exfoliated MoS_2, Nano Lett. **11**, 5111 (2011).

[29] A. A. Jeffery, C. Nethravathi, and M. Rajamathi, Two-dimensional nanosheets and layered hybrids of MoS_2 and WS_2 through exfoliation of ammoniated MS_2 (M = Mo, W), J. Phys. Chem. C **118**, 1386 (2014).

[30] V. S. Gorelik, A. V. Igo, S. N. Mikov, Raman scattering of light in small crystals, Zh. Éksp. Teor. Fiz. **109**, 2141 (1996) [J. Exp. Theor. Phys. **82**, 1154 (1996)].

[31] G. L. Frey, R. Tenne, M. J. Matthews, M. S. Dresselhaus, and G. Dresselhaus, Raman and resonance Raman investigation of MoS_2 nanoparticles, Phys. Rev. B **60**, 2883 (1999).

[32] G. Kresse and D. Joubert, From ultrasoft pseudopotentials to the projector augmented-wave method, Phys. Rev. B **59**, 1758 (1999).

[33] A. Fonari and S. Stauffer, vasp_raman.py [https://github.com/raman-sc/VASP/ (retrieved 2013)].

[34] M. Gajdoś, K. Hummer, G. Kresse, J. Furthmüller, and F. Bechstedt, Linear optical properties in the projector-augmented wave methodology, Phys. Rev. B **73**, 045112 (2006).

[35] C. Lee, H. Yan, L. Brus, T. Heinz, J. Hone, and S. Ryu, Anomalous lattice vibrations of single- and few-layer MoS_2, ACS Nano **4**, 2695 (2010).

[36] See Supplemental Material at http://link.aps.org/supplemental/10.1103/PhysRevApplied.7.024001 for a test calculation of defect-induced Raman spectra for bulk systems.

[37] Unfortunately, the experimental Raman intensities for our bilayer system (Fig. 2) cannot be compared directly with either our bulk experiment or the calculated intensities because the chemically exfoliated MoS_2 flakes exhibit a variety of skewed orientations with respect to the incident photoirradiation.

[38] N. S. McIntyre, P. A. Spevack, G. Beamson, and D. Briggs, Effects of argon ion bombardment on basal plane and polycrystalline MoS_2, Surf. Sci. **237**, L390 (1990).

[39] M. A. Baker, R. Gilmore, C. Lenardi, and W. Gissler, XPS investigation of preferential sputtering of S from MoS_2 and determination of MoS_x stoichiometry from Mo and S peak positions, Appl. Surf. Sci. **150**, 255 (1999).

[40] K. Santosh, R. C. Longo, R. Addou, R. M. Wallace, and K. Cho, Impact of intrinsic atomic defects on the electronic structure of MoS_2 monolayers, Nanotechnology **25**, 375703 (2014).